

Local phase relationship between sea surface temperature and net heat flux over weekly to annual periods in the extratropical North Pacific

Kohtaro Hosoda

Received: 22 February 2012 / Revised: 28 June 2012 / Accepted: 28 June 2012 / Published online: 28 July 2012
© The Oceanographic Society of Japan and Springer 2012

Abstract The relationship between sea surface temperature (SST) and net heat flux (NHF) in the North Pacific over weekly to annual period bands was investigated using gridded datasets of SST obtained by the Advanced Microwave Scanning Radiometer for the Earth Observing System, and flux data produced by the Modern-era Retrospective-analysis for Research and Applications Reanalysis. This study focused on the phase difference between the SST and NHF, which can suggest the driving force between two co-varying parameters. The SST delay behind the NHF, with phase differences from $\pi/4$ to $\pi/2$, which suggests that the SST change would be controlled by the NHF, was commonly found over all periods. In the intra-annual (100- to 200-day periods) band, part of the coherent variations showed negative phase differences (around $-\pi$ to $-\pi/3$), which were found in the western North Pacific and along $\sim 30^\circ\text{N}$ in the central North Pacific. The spatial scales of SST variability in the shorter band (weekly to intraseasonal: less than 100-day periods) are dominantly over 200 km. In contrast, the scales in the intra-annual band were in the range 50–150 km, where the negative phase differences were frequently found.

Keywords Sea surface temperature · Air–sea interaction · Wavelet transform

1 Introduction

Sea surface temperature (SST) fields involve various phenomena of wide-ranging spatial–temporal scales, which consist of air–sea heat exchanges, variability in upper oceans including eddies and currents, and vertical mixing by atmospheric turbulence and astronomical tides. The SST fields are fundamentally important for atmospheric and oceanographic applications and research. For monitoring systems or initial/boundary conditions for both atmospheric and oceanographic numerical models, the SST dataset without data gaps has been required, with high spatial [O (10 km) or less] and temporal [O (daily) or diurnal cycle-resolved] resolutions (The GHRSSST-PP User Requirements Documents, 2009; Eyre et al. 2009)

Infrared measurements of SST from space have been widely used to obtain SST gridded datasets since 1980s (e.g., McClain et al. 1985). However, SST values under clouds are not available from these infrared sensors, since infrared radiation from the sea surface cannot transmit through cloud droplets. Microwave SST measurements from space, which can provide sea surface information under clouds, were essentially required to resolve this cloud-masking problem and produce relatively high resolution datasets. Based on the tropical and global SST observations by space-borne microwave radiometers [Tropical rainfall measuring mission (TRMM) microwave imager (TMI) and Advanced Microwave Scanning Radiometer for the Earth Observing System (AMSR-E)] from 1997 and 2002, respectively, it became possible to produce cloud-free SST data with approximately 50-km spatial resolution. By merging the infrared [spatial resolution $\sim O$ (1 km)] and microwave observations, small-spatial grid [$\sim O$ (10 km) or less] SST products without data gaps have been produced and released for both regional (e.g., He

K. Hosoda (✉)
Center for Atmospheric and Oceanic Studies,
Graduate School of Science, Tohoku University,
6-3 Aramaki aza Aoba, Aoba, Sendai 980-8578, Japan
e-mail: hosoda@ocean.caos.tohoku.ac.jp

et al. 2003; Guan and Kawamura 2004; Sakaida et al. 2009) and global areas (e.g., Kawai et al. 2006; Reynolds et al. 2007) in the last decade.

To produce such SST datasets from several satellite remote-sensing observations, an optimal interpolation (OI) technique has been widely adopted. In the OI procedure, if the covariance function used in the interpolation process is equivalent to the covariance of the data fields, the dataset obtained by interpolation is optimal in the sense that the mean square error of the estimates is minimized (Emery and Thomson 2001). Early efforts to estimate these covariance functions for SST (e.g., Reynolds and Smith 1994; Reynolds et al. 2002) specifically addressed relatively long-term (annual to interannual) variability. Since the annual and basin-scale signals were dominant in SST variability, the SST fields produced from these covariances (in which spatial and temporal scales are larger than 500 km and a few months, respectively) were extremely smoothed.

By removing the annual signal from the SST time series, Hosoda and Kawamura (2004, 2005) estimated decorrelation scale for the SST anomaly from AMSR-E data, and derived spatial and temporal scales of 150–200 km and 2–7 days, respectively. In addition, this research reported that decorrelation scales involved seasonal changes; i.e., in summer, large spatial and short temporal scales were predominant, while in winter, small spatial and long temporal were prevalent. It was suggested that the former state would reflect SST changes affected by atmospheric disturbances with large spatial [O (several hundred kilometers)] and short temporal scales [O (weekly or intra-seasonal)], and that the latter state would be influenced by oceanographic disturbances which would be relatively slow to vary and have small spatial scales. The Japan Meteorological Agency (JMA) attempts the following scale-dividing method in their OI procedure [Merged Global Daily SST (MGDSST); Sakurai et al. 2005], to maintain information for the various scales of SST disturbances. First, the SST data are decomposed into different spatial and temporal scales with band-pass filter; next, OI is applied to each decomposed time series individually; and, finally, all are integrated to produce the full SST time series. Iwasaki et al. (2008) pointed out that the MGDSST dataset provided the best quality among the global infrared/microwave merged SST products that were available at that time. These previous studies demonstrated that the scale-dividing method for OI would be effective in the production of high-resolution SST datasets. However, it was not clear which period or wavelength should be selected for scale division. For this sophisticated merging method, knowledge of the appropriate cut-off frequency, at which phenomena induced by different sources should predominate, would form the basis for scale division selection.

Using observations from moored buoys around Japan, Murakami and Kawamura (2001) investigated the relationship between SST and sea surface net heat flux (NHF). It was suggested that the SST variability would be determined predominantly by atmospheric forcing over very short and annual periods, and that for intermediate periods, a part of the SST variability would affect flux. This result was highly suggestive of an appropriate cut-off frequency for the merging technique with scale division; the SST variability at intermediate periods would be partially driven by oceanic disturbances, which were expected to occur on relatively small spatial scales. However, since their analysis was based on a time series of SST and NHF at a few locations, the applicability of these relationships in other areas has not been determined. To address these issues, gridded datasets with relatively high spatial–temporal resolutions, which can at least capture the spatial distribution of oceanic eddies (ocean-eddy-permitting scale), have been required for both SST and NHF in broad areas.

The purpose of this study was to clarify the predominant relationship between SST and air–sea heat exchange in time and period of fluctuations. The information obtained from this analysis could be helpful for the optimal solution of the scale-dividing method in OI SST production. The analyzed area in this study was the North Pacific (20–65°N, 100°E–100°W) and the analysis period was from 2003 to 2010.

The remainder of this paper is organized as follows. Section 2 describes an outline of the datasets. A theoretical background of air–sea heat exchange and an analysis method will be given in Sect. 3. Section 4 shows the results from this study. Our summary and its related discussions are presented in Sect. 5.

2 Data

The AMSR-E was a multi-channel scanning passive microwave radiometer, and its 6.925-GHz channels, at which the effective spatial resolution was about 40×70 km, were mainly used for estimating SST. Since the low-frequency (6–10 GHz) microwaves could penetrate the clouds, global SST fields without data gaps were available with relatively high temporal resolution (3 days) by AMSR-E (Hosoda 2010; Fig. 1). The AMSR-E was launched on 4 May 2002, and operation continued until 4 October 2011, when the AMSR-E stopped functioning due to a problem with antenna rotation (http://www.jaxa.jp/press/2011/10/20111004_amsr-e_e.html). A basic description of the AMSR-E SST retrieval algorithm, and improved correction methods for winds and atmospheric stability, were given by Shibata (2004, 2006, 2007). For this study, we used the Version-6 Level-3 AMSR-E SST dataset, in which these improvements were adopted.

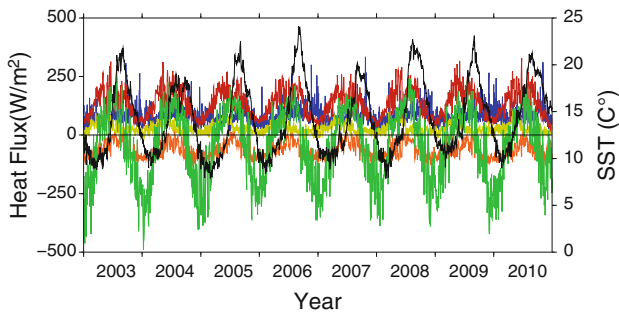


Fig. 1 Time series of SST (*black line*) and surface heat fluxes in the central mid-latitude North Pacific (40°N, 170°E) from AMSR-E and MERRA data. The net downward heat flux (NHF) is shown as a *thick green line*, and its components are drawn in *thin lines* *blue* upward latent turbulent flux Q_{LH}^{\uparrow} , *yellow* upward sensible turbulent flux Q_{SH}^{\uparrow} , *red* net shortwave radiation (downward positive: Q_{SWn}^{\downarrow}), and *orange* net longwave radiation (downward positive: Q_{LWn}^{\downarrow})

The spatial grid in the original Level-3 product was $0.25^{\circ} \times 0.25^{\circ}$. For comparison with the reanalysis data described below, the AMSR-E data were averaged in $1/2^{\circ}$ latitude \times $2/3^{\circ}$ longitude spatial grids, and then a 1-day-interval time series at each grid was provided using a 3-day running average window to fill the data gaps. An optimal interpolation method, which has been widely used for producing gridded SST datasets with $O(>100 \text{ km})$ spatial de-correlation scales in this decade, was not adopted in this study to keep the mesoscale variability in the data.

The Modern-era Retrospective-analysis for Research and Applications (MERRA) is the latest reanalysis for the atmosphere produced by the National Aeronautics and Space Administration (NASA) Goddard Space Flight Center (GSFC) Global Modeling and Assimilation Office (GMAO), using the Goddard Earth Observing System (GEOS) Data Assimilation System (DAS). For the boundary conditions of the ocean surface, the weekly- and 1° -resolution OI SST product of Reynolds et al. (2002) was adopted (Rienecker et al. 2011). From the many types of atmospheric variables in the MERRA dataset, this study used the surface turbulent flux (tavgl_2d_flux_Nx) and radiation flux (tavgl_2d_rad_Nx) data collections, which are provided with a horizontal resolution of $1/2^{\circ}$ latitude \times $2/3^{\circ}$ longitude and a 1-h temporal resolution. The MERRA data were obtained through the MERRA Data Holding website (<http://disc.sci.gsfc.nasa.gov/daac-bin/DataHoldings.pl>). For evaluation of the available surface turbulent flux gridded datasets, Brunke et al. (2011) compared MERRA and other global flux products with direct flux measurements by ships over the tropics, mid- and high latitudes. The datasets evaluated by them consisted of atmospheric reanalysis, satellite-derived, and their combined products. They concluded that MERRA performed the best for the ocean surface fluxes among these gridded surface flux datasets. For comparison with the AMSR-E SST data in

this study, the MERRA time series were averaged in 1-day temporal steps. The 3-day running mean, which was adopted in the AMSR-E SST for filling, was not applied to the MERRA time series. With and without the running mean for MERRA, analyzed results were not very different over a longer fluctuating period ($>$ weekly).

3 Theory and method of analysis

3.1 Relationship between SST and NHF

3.1.1 General framework

The NHF at the sea surface in this study was defined as the downward positive form Q_{net}^{\downarrow} as follows,

$$Q_{net}^{\downarrow} = Q_{SWn}^{\downarrow} + Q_{LWn}^{\downarrow} - Q_{SH}^{\uparrow} - Q_{LH}^{\uparrow}, \tag{1}$$

where Q_{SWn}^{\downarrow} and Q_{LWn}^{\downarrow} are the net shortwave and longwave radiations at the sea surface (downward positive), and Q_{SH}^{\uparrow} and Q_{LH}^{\uparrow} are the sensible and latent heat fluxes (upward positive). Here, we consider the temporal change of heat content in the upper ocean with depth D_B . The relationship between Q_{net}^{\downarrow} , the heat content in the upper ocean (OHC), horizontal advection contributions by geostrophic and non-geostrophic (e.g., Ekman) currents (A_v), vertical heat advection at the depth D_B (V_m), and dissipation effects by turbulence of vertical direction at the depth D_B and meridional/zonal directions (D_s) can be simplified as

$$\frac{\partial \text{OHC}}{\partial t} = Q_{net}^{\downarrow} + A_v + V_m + D_s, \tag{2}$$

$$\text{OHC} = \rho c_p \int_0^{D_B} T(z, t) dz, \tag{3}$$

where $T(z, t)$ is a water temperature profile in the upper ocean, z is the depth (positive downward), and ρ and c_p are the density and specific heat of sea water, respectively. The depth D_B should be set to be deeper than the maximum mixed layer thickness in all seasons. If the depth D_B is shallower than the maximum mixed layer thickness, heat exchange at sea surface could influence heat contents below the discussed upper ocean layer, which leads large V_m in Eq. (2). In the following interpretations for Eqs. (2) and (3), the advection term A_v , vertical processes V_m , and dissipative term D_s in Eq. (2) are neglected since the relationship between NHF and SST was focused in this study.

3.1.2 Cayan's (1992) model

The simplest interpretation of Q_{net}^{\downarrow} and SST relationship from Eq. (2) is as follows, which was introduced by Cayan

(1992). If OHC is assumed to be proportional to SST as $OHC(t) = c_p \rho D(t)SST(t)$, $D(t)$ gives a depth scale for the mean depth value of the upper-layer temperature profile:

$$D(t) = \frac{1}{SST} \int_0^{D_B} T(z, t) dz. \quad (4)$$

When the temporal change of $D(t)$ is neglected ($D(t) = D$), Eq. (2) without forcing terms except for Q_{net}^{\downarrow} can be transformed to the following relationship between the SST temporal change (SST tendency) and Q_{net}^{\downarrow} :

$$\frac{\partial SST}{\partial t} = \frac{Q_{net}^{\downarrow}}{c_p \rho D}. \quad (5)$$

Figure 1 shows an example of Q_{net}^{\downarrow} and SST timeseries at 40°N, 170°E. For the annual cycle, which is dominant in both SST and Q_{net}^{\downarrow} , the positive peaks of SST lagged behind those of the downward NHF (Q_{net}^{\downarrow}) by 1–2 months. This delay in SST change reflected the relationship described in Eq. (5). Focusing on the interannual variability, Cayan (1992) introduced this relationship (Eq. (5)) and discussed the local response of SST tendency to the heat flux in the Northern Hemisphere. Wu and Kinter (2010) showed the east–west contrast and seasonal change of the relationship between them in the North Pacific. According to other atmospheric parameters, for example, Deser and Timlin (1997) showed the coupled pattern of SST tendency and 500-hPa height. Many studies (e.g., Liu et al. 1994; Fu et al. 1996; Shinoda et al. 1998; Chou and Hsueh 2010; Wang et al. 2012) have focused on the SST tendency and atmospheric parameters, including surface heat flux, for discussing the relationship between SST and atmosphere. Wallace et al. (1990) pointed out that the interpretation of the atmospheric variables and SST tendency was more straightforward compared to those between the atmosphere and SST itself.

However, it is difficult to acquire one optimum solution to define an appropriate temporal step Δt for calculating the finite-difference approximation of the SST tendency $\partial SST / \partial t$ as $\Delta SST / \Delta t$ for all periods of various variations. Because of their focus on the interannual and annual variability, Cayan (1992) and Wu and Kinter (2010) used the centered difference from the monthly mean SST fields for extracting the SST tendency at each grid. On the other hand, Deser and Timlin (1997) calculated the SST tendency as its change in ± 2 weeks, since their focus was the weekly time scale. Since this study attempts to analyze the air–sea relationship over various time scales, the approach using the SST tendency was not adopted.

For convenience, both Q_{net}^{\downarrow} and SST are expanded into Fourier series as $Q_{net}^{\downarrow} = \sum_{\omega} Q_{SWn}^{\downarrow}(\omega) e^{i\omega t}$ and $SST = \sum_{\omega} SST_s(t, \omega) = \sum_{\omega} SST_0(\omega) e^{i\omega t}$ ($i = \sqrt{-1}$). Substituting on Eq. (5) gives the following relationship:

$$SST_s(t, \omega) = \frac{1}{\omega c_p \rho D} Q_0^{\downarrow}(\omega) e^{i(\omega t - \pi/2)}, \quad (6)$$

which indicates that the temporal change of the SST is behind the Q_{net}^{\downarrow} change by a phase difference of $\pi/2$, if the SST change is driven by atmospheric forcing at the frequency ω .

At this point, it is necessary to discuss the assumption of neglecting temporal change of the depth scale $D(t)$ in the above derivation. Assuming that the temperatures in surface mixed layer are same as SST with an exponential profile below the surface mixed layer, vertical profile of temperature $T(z)$ can be expressed as,

$$T(z) = \begin{cases} SST & (0 \leq z \leq D_M), \\ T_0 e^{\gamma z} & (D_M \leq z \leq D_B), \end{cases} \quad (7)$$

where $D_M = D_M(t)$ is the thickness of the mixed layer, and γ ($\gamma < 0$) and T_0 are constant parameters describing stratification below the mixed layer. Substituting Eq. (7) into Eq. (4), the depth scale is given by,

$$\begin{aligned} D(t) &= D_M + \frac{T_0}{\gamma} [e^{\gamma D_B} - e^{\gamma D_M}] \\ &= D_M + \frac{1}{\gamma} \left[\frac{T(D_B)}{SST} - 1 \right], \end{aligned} \quad (8)$$

where $T(D_B)$ is the temperature at the bottom of layer for calculating OHC. Since the framework in this study considers surface flux only, if the depth D_B is deep enough to be free from surface forcing, it is reasonable to assume that $T(D_B)$ is constant.

The temporal change of $D(t)$ is mainly dependent on the mixed layer depth $D_M(t)$ and stratification under the mixed layer parametrized by γ . For annual cycle of SST, heat content (OHC) and potential energy in the upper layer with a constant depth, Gill and Turner (1976) gave an analytical solution for them including temporal change of mixed layer depth. From their heating-up season's solution for well-developed mixed layer structure by mechanical mixing, SST rising would stop after the positive peak of OHC temporal change by phase difference of $\pi/2$. The positive peak of OHC temporal change corresponds to the positive peak of Q_{net}^{\downarrow} in the framework of this study. They also showed that the analytical solution was consistent with the 4-year surface temperature profile data of 250 m depth obtained by ships at a fixed point in the North Atlantic. Therefore, it seems reasonable to suppose that phase difference $\pi/2$ between Q_{net}^{\downarrow} and SST could be indicative of the SST change controlled by the Q_{net}^{\downarrow} for the annual cycle, even if the mixed layer change is not negligible.

Next, let us turn to the assumption of constant $D(t)$ for shorter-temporal-scale changes of OHC than the annual cycle. From the left hand side of Eq. (2), we obtain

$$\begin{aligned} \frac{1}{c_p \rho} \frac{\partial \text{OHC}}{\partial t} &= \frac{\partial}{\partial t} \text{SST}(t) D(t) \\ &= \left(D_M - \frac{1}{\gamma} \right) \frac{\partial \text{SST}}{\partial t} + \text{SST} \frac{\partial D_M}{\partial t}. \end{aligned} \tag{9}$$

This equation means that the OHC temporal change is given by the mixed layer depth D_M , SST and vertical structure of the temperature below the mixed layer described by γ . It should be noted that the temporal change of OHC is not dependent on the depth of layer D_B in this simplified model. A slow-varying time τ in addition to normal time t is introduced for describing fast- and slow-varying parts for D_M and SST as $D_M = \widehat{D}_M(\tau) + D'_M(t)$ and $\text{SST} = \widehat{\text{SST}}(\tau) + \text{SST}'(t)$. The slow-varying part $\widehat{D}_M(\tau)$ and $\widehat{\text{SST}}(\tau)$ represent their annual cycles, whose amplitudes are dominant in their variability. This assumption gives that the quadratic terms of fast-varying part, $D'_M \text{SST}'$, is negligible in the discussion. The OHC temporal change for time t can be rewritten as,

$$\frac{1}{c_p \rho} \frac{\partial \text{OHC}}{\partial t} = \left(\widehat{D}_M(\tau) - \frac{1}{\gamma} \right) \frac{\partial \widehat{\text{SST}}}{\partial t} + \widehat{\text{SST}}(\tau) \frac{\partial D'_M}{\partial t}. \tag{10}$$

Introducing the slow-varying depth scale $\widehat{D}(\tau) \equiv \widehat{D}_M(\tau) - \gamma^{-1}$, we obtain the SST tendency equation (Eq. (5)) as,

$$\frac{\partial \text{SST}'(t)}{\partial t} = \frac{Q_{\text{net}}^\downarrow(t)}{c_p \rho \widehat{D}(\tau)} - \frac{\widehat{\text{SST}}}{\widehat{D}(\tau)} \frac{\partial D'_M}{\partial t}.$$

The second term in the right hand side can be neglected if the following condition is satisfied;

$$\frac{1}{\widehat{D}_M(\tau) - 1/\gamma} \frac{\partial D'_M}{\partial t} \ll 1. \tag{11}$$

Under this condition, the SST tendency equation with constant depth scale D (Eq. (5)) can be obtained for fast-varying part, since temporal change of slow-varying depth scale \widehat{D} is negligible in the fast-varying equation. This condition implies that if (1) the background mixed layer depth $\widehat{D}_M(\tau)$ is large enough, or (2) the stratification below the mixed layer $-1/\gamma$ is strong enough, the mixed layer depth temporal change in short-term variation $D'_M(t)$ is negligible. Since the amplitude $\widehat{D}_M(\tau)$ of annual cycle would be dominantly large compared to the shorter-temporal-scale changes of mixed layer depth in usual, the condition (Eq. (11)) would be expected to be satisfied in the oceans.

The appropriateness of this condition should be confirmed by using oceanographic data in future studies. In this study, we limit the discussion to the $Q_{\text{net}}^\downarrow$ -SST linear relation with the assumption of constant D .

3.1.3 D-model

Another interpretation of $Q_{\text{net}}^\downarrow$ and SST relationship from Eq. (2) without forcing terms except for $Q_{\text{net}}^\downarrow$ was given by Murakami and Kawamura (2001), which was based on the so-called D-model developed by Warren (1976) for describing surface heat content in heating seasons. Heat transmission from the ocean surface into deeper layers via turbulence was taken into consideration in the mixed layer model. The vertical heat diffusion can be represented by the constant eddy diffusivity K ($\text{m}^2 \text{s}^{-1}$),

$$\frac{\partial T(z, t)}{\partial t} = K \frac{\partial^2 T(z, t)}{\partial z^2}. \tag{12}$$

The eddy diffusivity expression $K \partial T / \partial z$ is introduced to parametrize the vertical heat flux by turbulence $\overline{w'T'}$, where w' and T' are vertical velocity and temperature fluctuations induced by smaller turbulence (Thorpe 2007). From Eqs. (2) and (3) with neglecting forcing terms excepting $Q_{\text{net}}^\downarrow$, the relationship between $T(z, t)$ and $Q_{\text{net}}^\downarrow$ is described as

$$\rho c_p \int \frac{\partial T(z, t)}{\partial t} dz = Q_{\text{net}}^\downarrow. \tag{13}$$

The boundary conditions at the surface and deep ocean are given as

$$\frac{\partial T(z, t)}{\partial t} \rightarrow 0 \quad \text{at } z \rightarrow \infty, \tag{14}$$

$$T(0, t) = \text{SST}(t). \tag{15}$$

As previously discussed, $Q_{\text{net}}^\downarrow$ is expanded into Fourier series and forcing terms except for $Q_{\text{net}}^\downarrow$ in Eq. (2) are neglected. For the vertical temperature profile, the Fourier expansion with assumption of exponential vertical profile is adopted as $T(z, t) = \sum_{\omega} T_0 e^{\alpha z} e^{i\omega t}$.

Substituting these expansions into Eqs. (2), (3) and (12) with boundary condition of Eq. (14), the parameters α and T_0 are given as,

$$\alpha = -(1 + i) \sqrt{\frac{\omega}{2K(\omega)}}, \tag{16}$$

$$T_0 = (1 - i) \frac{Q(\omega)}{\omega \rho c_p} \sqrt{\frac{\omega}{2K(\omega)}}, \tag{17}$$

where $K(\omega)$ is the eddy diffusivity at each frequency ω .

This expression is predicated on the following: the scales of T' and w' , which contribute eddy diffusion to the fluctuation with frequency ω , should be shorter than those that are of direct interest in discussing frequency ω . The threshold for dividing these scales would be determined by the frequency ω itself. Therefore, eddy diffusion K , which is introduced for parametrization of $\overline{w'T'}$, would be a function of ω .

Substituting these parameters into Eq. (15), the SST equation is given as,

$$\text{SST}_s(t, \omega) = \frac{1}{c_p \rho} \sqrt{\frac{\omega}{K(\omega)}} Q_0(\omega) e^{i(\omega t - \pi/4)}. \quad (18)$$

This equation advocates that the phase difference between the SST and $Q_{\text{net}}^{\downarrow}$ would be $\pi/4$ if $Q_{\text{net}}^{\downarrow}$ drives the SST change.

3.1.4 Summary of theoretical hypotheses

The approach using the phase difference for analysis of the air–sea local relationship has the advantage of being free from the problem of temporal step in the SST tendency approach. Konda et al. (1996) studied the phase difference between SST and the latent and sensible heat fluxes for describing which controls the biennial variation of the air–sea interaction. Wang and Enfield (2001) discussed the phase difference between NHF and SST for annual variation in the tropics. This study adopts the phase-difference approach to describe the relationship between SST and $Q_{\text{net}}^{\downarrow}$ for various temporal scales.

The Eq. (6) and phase difference $\pi/2$ would correspond to SST variability accompanied by well-developed mixed layer, since the OHC would be well correlated with its overlaying SST in such a condition. Therefore, the cooling-down phase of the surface layer ($\partial\text{OHC}(\omega)/\partial t < 0$) would be characterized by Eq. (6) and phase difference $\pi/2$. The Eq. (18) and phase difference $\pi/4$ would correspond to the heating-up phases ($\partial\text{OHC}(\omega)/\partial t > 0$), in which very shallow stratification within the uppermost several meters to tens of meters depth is formed. However, in longer time-scale changes, the mechanical mixing by winds or buoyancy effects by atmospheric cooling, with a shorter time scale than that of the discussed time scale ω^{-1} , would destroy the very shallow stratification within the appropriate time step Δt for the time scale ω^{-1} (e.g., monthly time step Δt for annual cycle; e.g., Cayan 1992; Wu and Kinter 2010). An approximation using a mixed layer structure with the same temperature as SST could be applied to such time scales even in heating-up phases. On the other hand, the relationship of Eq. (18) and phase difference $\pi/4$ would be possible if the vertical mixing mechanisms by atmosphere did not occur in a cycle of the discussed frequency ω . Consequently, the phase difference $\pi/4$ would be found more frequently in the shorter time scales than in the longer time scales, and the phase differences in the longer time scales would be concentrated near $\pi/2$. While it could be one of the cut-off frequencies for scale-division for the OI procedure, we are not concerned in this study with this phase change in time scales, since the data processing (3-day running mean for SST) and weekly OISST used in reanalysis data would obscure the phase changes in short time scales.

In this study, the positive phase differences around $[\pi/4, \pi/2]$ between $Q_{\text{net}}^{\downarrow}$ and SST will be regarded as an indication of SST change controlled by $Q_{\text{net}}^{\downarrow}$, as a whole. This paper is intended as an investigation of their relationships with negative phase differences, which suggests that as the SST change would be controlled by other effects (A_v , V_m and D_s in Eq. (2)). These SST changes controlled by oceanic forcing would have small-spatial-scale features. The periods of fluctuations, seasons and areas with these negative phase differences come within the scope of this paper.

3.2 Wavelet transform

We employed a wavelet transform to decompose the $Q_{\text{net}}^{\downarrow}$ and SST time series in order to investigate their temporal characteristics. Wavelet analysis can provide information about localized power variations within a time series. The Morlet mother wavelet was adopted in this study. Torrence and Compo (1998) and Murakami and Kawamura (2001) introduced wavelet analysis for oceanographic data. Torrence and Webster (1999) and Grinsted et al. (2004) introduced a calculation method for the cross wavelet transform, wavelet squared coherency, and phase difference $\delta\theta$ from two time series for comparison.

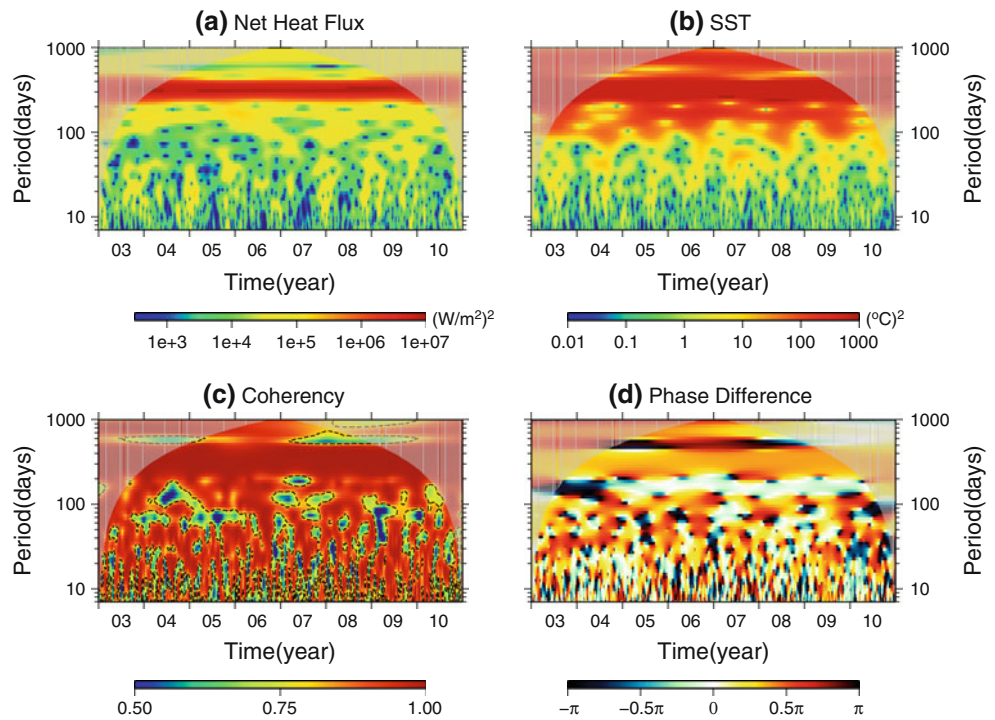
In this study, a positive phase difference, $\delta\theta > 0$, was defined as the SST change lagged behind the downward NHF ($Q_{\text{net}}^{\downarrow}$). The wavelet squared coherency is used to identify both the frequency band and time intervals within which two time series are co-varying. Hereafter, the term “wavelet coherency” refers to the wavelet squared coherency.

As indicated by Eqs. (6) and (18), a positive phase difference $\delta\theta > 0$ around $\delta\theta = \pi/4$ to $\pi/2$, therefore, can be expected as an indication of atmospheric control of the SST during the period and time of the wavelet analysis.

Figure 2 shows an example of the wavelet power spectra for $Q_{\text{net}}^{\downarrow}$, SST, wavelet coherency, and $\delta\theta$ between them, which were obtained from time series at 40°N, 170°E. The shaded area in time-frequency space indicates a “cone-of-influence”, in which zero padding influenced the variance. In the following section, the wavelet analysis from 2004 to 2009 will be discussed to avoid any edge effects of the time series. Those in periods shorter than a weekly cycle are not shown, since the 3-day running mean in the SST time series reduced the variability in the shorter period bands. The variances at intra-seasonal to semi-annual (about 200-day) period bands showed interannual changes in both $Q_{\text{net}}^{\downarrow}$ and SST. At the annual cycle, $Q_{\text{net}}^{\downarrow}$ and SST showed significant coherency for all the analyzed time periods. For the most parts, at the intra-seasonal to semi-annual bands, the wavelet coherency was higher than 0.8, with some intervals of low coherency. Phase differences were generally positive, which means that SST changes lagged behind those of

Fig. 2 Examples of wavelet transform for SST and NHF from AMSR-E and MERRA time series at 40°N, 170°E.

a, b Wavelet power spectra (using the Morlet wavelet) of the downward NHF and SST, respectively. The shaded regions indicate the “cone-of-influence”, in which zero padding reduced the variance. **c, d** The wavelet coherency and phase difference between the downward NHF and SST. The broken contour is the 5% significance level from a Monte Carlo simulation of wavelet coherency between 10,000 sets of a white-noise time series. A positive phase difference means that the downward NHF changes led those of SST



$Q_{\text{net}}^{\downarrow}$, while negative phase differences were found in part of the intra-seasonal to semi-annual bands. In the following section, only the phase differences when the wavelet coherency was significant will be discussed.

3.3 EM + GMM clustering

Usually, the phase difference and its seasonal dependence between $Q_{\text{net}}^{\downarrow}$ and SST are gradually distributed without an apparent boundary, where the relationships between them are drastically changed. For classifying the results from wavelet analysis, an expectation-maximization (EM) + Gaussian mixture model (GMM) clustering (Bilmes 1998) was adopted in this study. A mixture model M , which has K clusters identified by $C_l (l = 1, \dots, K)$ in the model, assigns a probability to a data point described by a d -dimensional vector \mathbf{x} as follows:

$$P(\mathbf{x}|M) = \sum_{l=1}^K W_l p(\mathbf{x}|C_l, M), \tag{19}$$

where W_l is the relative weight of cluster C_l in the model ($\sum_l W_l = 1$), and $p(\mathbf{x}|C_l, M)$ is the density function of cluster C_l . In this study, the individual component densities of the mixture model are assumed to be multi-variate Gaussians (GMM):

$$p(\mathbf{x}|C_l, M) = \mathcal{N}(\mathbf{x}|\mu_l, \Sigma_l) = \frac{1}{(2\pi)^{d/2} |\Sigma_l|^{1/2}} \exp \left[-\frac{1}{2} (\mathbf{x} - \mu_l)^T \Sigma_l^{-1} (\mathbf{x} - \mu_l) \right], \tag{20}$$

where μ_l is a d -dimensional mean vector and Σ_l is $d \times d$ covariance matrix of the cluster C_l . For the core area of each cluster, we define the interior of the ellipse by the relation $1/2(\mathbf{x} - \mu_l)^T \Sigma_l^{-1} (\mathbf{x} - \mu_l) = 1$. In this study, the data points from the wavelet coherent analysis are distributed on the plane of the phase difference $\delta\theta$ between $Q_{\text{net}}^{\downarrow}$ and SST, and season (day-of-year: DY): $d = 2$ and $\mathbf{x} = (\delta\theta, \text{DY})^T$. Note that both dimensions are cyclic in this case. Covariance matrix Σ_l^{-1} for each cluster was given by variances of $\delta\theta$ and DY ($\sigma_{\delta\theta}^2, \sigma_{\text{DY}}^2$) and covariance between them $\sigma_{\delta\theta, \text{DY}}$. The number of clusters K was determined by the statistical criteria described later. The EM algorithm finds locally optimal solutions maximizing the likelihood of the data given in the model. GMM parameters (mean μ_l , covariance matrix Σ_l and weight W_l) are computed by EM as follows:

1. Initialize the mixture model parameters, producing a current model. The number of estimated clusters K is assumed at this initial step.
2. E-step: compute posterior probabilities of data items, assuming the current model (Eqs. (19) and (20)).
3. M-step: update the model parameters (μ_l, Σ_l , and W_l) based on posterior probabilities from the 2nd step. A new model is produced.
4. If the current and new models are sufficiently close, terminate the process. If not, go back to step 2.

To determine the convergence at the 4th step, the Bayesian Information Criterion (BIC; Schwarz 1978) was used. The BIC is defined as,

$$\text{BIC} = -2 \ln L + k \ln N, \quad (21)$$

where $\ln L$ is the log-likelihood function of all the clusters, N is the number of data points, and k is the number of the parameters to be estimated, which is proportional to the number of clusters K in each iterative estimation. The iteration is stopped if the difference of the BIC between the current and the next model is small enough. The obtained local minimum BIC, which would be dependent on the initial parameters, is checked by iteration results starting from several different initial parameters.

From the final BIC scores of iterations using all models ($K = 1, 2, 3, \dots$), the appropriate number of clusters K is selected under the condition of optimizing the BIC. The optimization of the BIC for giving the number of clusters in the estimation is a similar technique to that used in X-means clustering (Pelleg and Moore 2000), which improved the K-means clustering method by integrating automatic determination of the cluster number.

4 Results

The probability density functions (PDFs) of the phase relationship between the $Q_{\text{net}}^{\downarrow}$ and SST coherent variation for all periods for whole studied area are summarized in Fig. 3. The PDF was normalized by all the data, including both coherent and non-coherent variations in each period. Except for an annual cycle band, the coherent variations between them account for about 50–60 % of the total. An exception was found in the 102-day period band, at which the ratio of coherent variation was less than 50 %. The decreases in the coherent variation in this band were mostly found (figure not shown) in the winter to early spring (January to May) in the Bering and Okhotsk Seas, in which the maximum ratio of incoherent variation in each spatial grid was up to 80 % in March. These remarkable seasonal changes were found in a period band from 102-day period to 132-day period. It would be associated with the freezing and melting of sea ice, which emits and absorbs heat fluxes without substantial surface temperature change at the beginning and end of the sea ice season, respectively.

Figure 4 shows the PDFs for five different areas in the North Pacific. The Kuroshio core area (Fig. 4a) was defined as the grid with a slope of mean absolute dynamic topography (Fig. 5b), which is available from Archiving, Validation and Interpretation of Satellite Oceanographic (AVISO), was larger than 30 cm/100 km. The PDFs shows regional dependencies in the various time scales. In the following, the regional dependencies will be described in detail for three time scale bands: (1) annual cycle (200- to 400-day period) band, (2) shorter (7-day to 100-day period) band, and (3) intra-annual (100- to 200-day period) band.

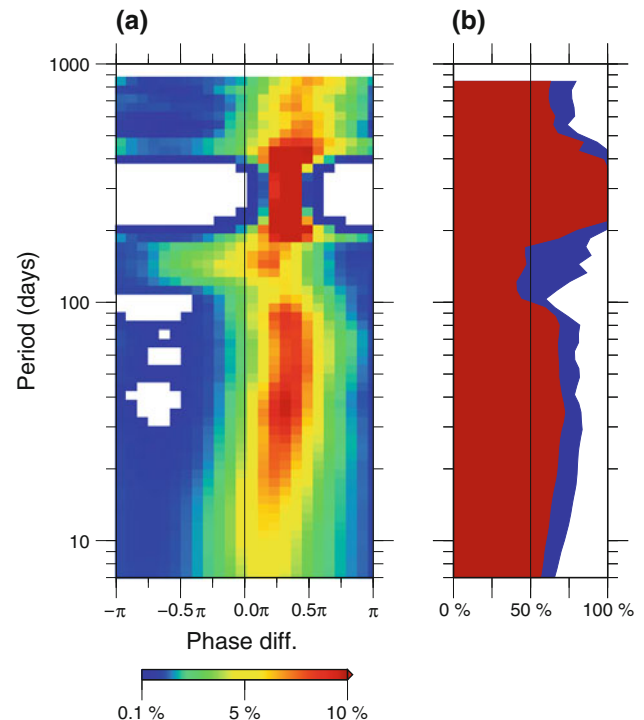


Fig. 3 PDFs of phase differences between NHF and SST for all periods. **a** Frequency diagram of the phase difference between the downward NHF $Q_{\text{net}}^{\downarrow}$ and SST for whole area in this study. The color shows the ratio (percentage) of data with significant coherency in each $\pi/36$ -phase bin to the total data (2.65×10^7). **b** Red + blue the percentage of data with significant coherency to the total data number in each period. Red the percentage of data number with significant coherency and a positive ($\pi/5 - 2\pi/3$) phase difference, which suggests that NHF would control SST changes

The percent variances of each band were (1) 71.4 %, (2) 9.60 %, (3) 19.0 % for $Q_{\text{net}}^{\downarrow}$, and (1) 81.2 %, (2) 10.1 %, (3) 7.87 % for SST.

For the annual cycle (200- to 400-day period) band, all data show coherent variation between $Q_{\text{net}}^{\downarrow}$ and SST. The center of the PDF for the phase differences between them was located around $\pi/3$ and the width of the PDF was confined to the range of $[\pi/5, \pi/2]$. This suggests that the air–sea flux would principally control the SST annual cycle in the North Pacific. However, the distribution of the mean phase difference at each spatial grid (Fig. 5) suggested that ocean currents would be associated with the modulation of the annual SST cycle in particular areas. In the central and eastern North Pacific, the phase difference ranged from $2\pi/5$ to $\pi/2$. In contrast, the phase difference in the poleward currents (the Kuroshio and Alaska currents) was less than $2\pi/5$, and as low as $\pi/5$ in the areas around Taiwan and off the western coast of British Columbia and Washington states. While the poleward currents off the western coast of the US were not clear from the annual mean sea surface height (Fig. 5b), it is known that the poleward surface coastal current (Davidson current) is formed in

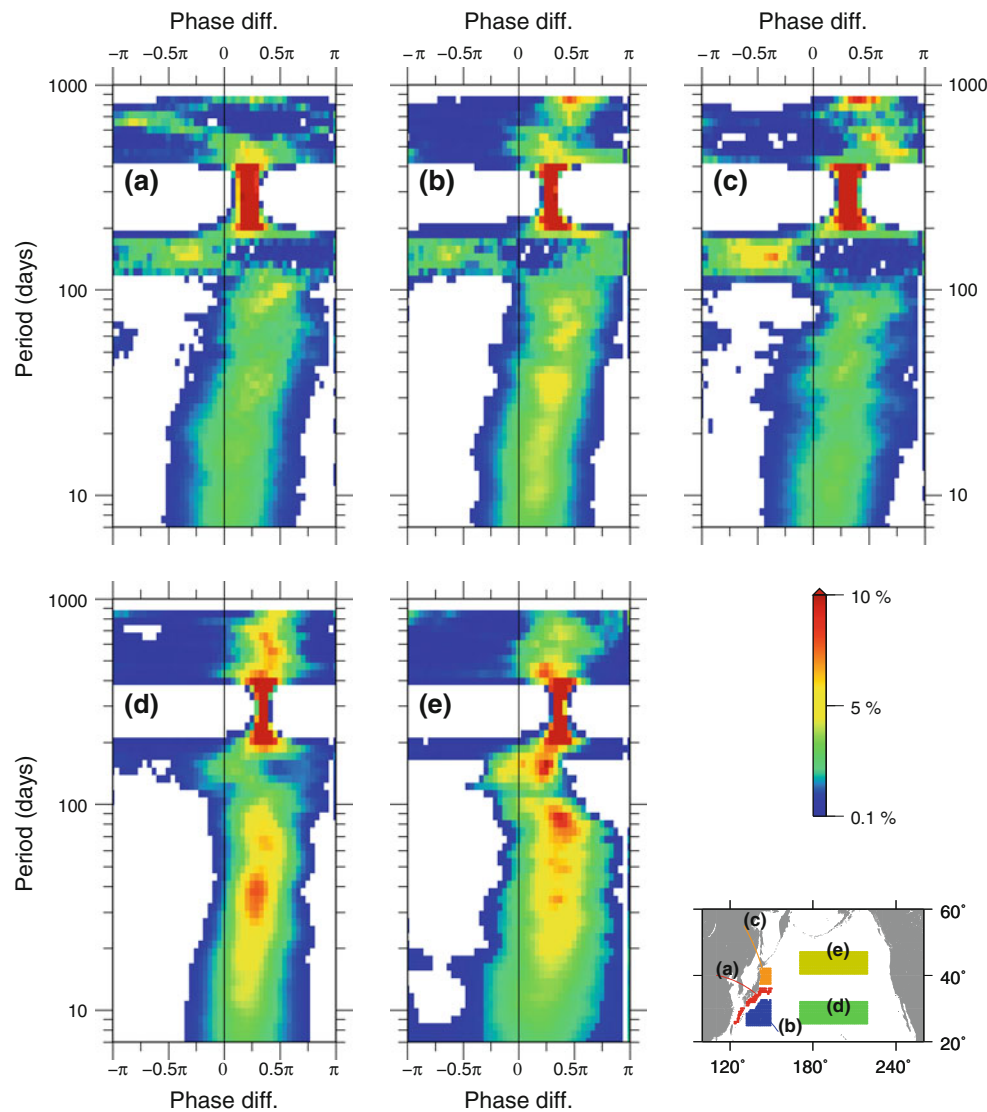


Fig. 4 Frequency diagram of the phase difference between the downward NHF $Q_{\text{net}}^{\downarrow}$ and SST for areas shown in the *bottom-right map*. **a** the Kuroshio core area (see text for area definition), **b** the Kuroshio recirculation region (south of Kuroshio and lat. $\geq 25^{\circ}\text{N}$,

$132^{\circ}\text{--}150^{\circ}\text{E}$), **c** the Kuroshio/Oyashio Mixed Water Region ($37^{\circ}\text{--}42.5^{\circ}\text{N}$, $140^{\circ}\text{--}150^{\circ}\text{E}$), **d** subtropical, and **e** subpolar areas ($25^{\circ}\text{--}32.5^{\circ}\text{N}$, $170^{\circ}\text{E}\text{--}140^{\circ}\text{W}$, and $40^{\circ}\text{--}47.5^{\circ}\text{N}$, $170^{\circ}\text{E}\text{--}140^{\circ}\text{W}$, respectively)

wintertime and flows from northern California to southern British Columbia (e.g., Hickey 1989). This suggests that the heat conveyed by the poleward currents could advance the seasonal progress of the SST by $\pi/10$ to $\pi/5$ (about 15–40 days) earlier than that driven by $Q_{\text{net}}^{\downarrow}$ alone.

In the shorter (less than 100-day period) band, the major part of the phase relationship between $Q_{\text{net}}^{\downarrow}$ and SST was concentrated in the positive phase difference, which implies that the SST variability would be controlled by $Q_{\text{net}}^{\downarrow}$ in this band. The coherent variations in this band were relatively more infrequent in the Kuroshio and Kuroshio/Oyashio Mixed Water Region (Fig. 4a, c) than those in the subpolar and subtropical oceans (Fig. 4d, e). A part of causes for these phenomena might be due to the strong currents and mesoscale eddy activity in these areas, which

would change SST by their heat advection. The advection effect would decrease the coherent variations between $Q_{\text{net}}^{\downarrow}$ and SST. Another cause might be due to the low-resolution SST used in the MERRA reanalysis for ocean surface boundary condition, which would blur the meso-scale or smaller structures of SST by currents and eddies (the Appendix gives the evaluation of the SST difference between Reynolds et al. (2002) and AMSR-E unfiltered data.). The SST errors in the low-resolution dataset might modify the heat fluxes to unrealistic values. As a result, the coherent variations between $Q_{\text{net}}^{\downarrow}$ and SST would be decreased in these areas.

The negative phase difference was extremely rare in the intra-seasonal (30- to 100-day periods) band. In the weekly to monthly (less than 30-day periods) band, the center

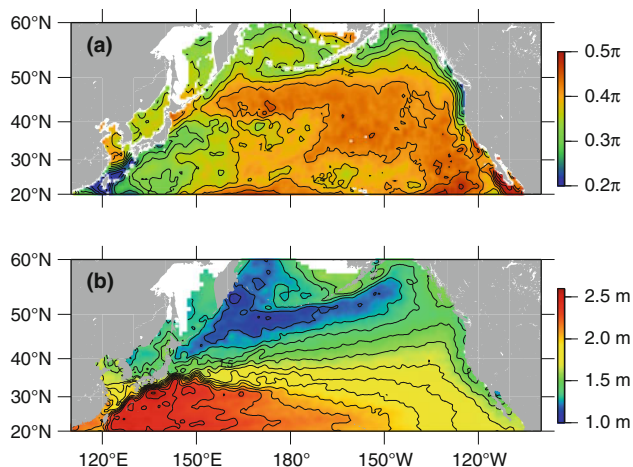


Fig. 5 Maps for annual cycle results. **a** Mean phase difference between the downward NHF $Q_{\text{net}}^{\downarrow}$ and SST of annual cycle at each spatial grid ($1/2^{\circ}$ lat. \times $2/3^{\circ}$ lon.). CI = 0.1 radian. **b** Mean absolute dynamic topography (2003–2009) from Archiving, Validation and Interpretation of Satellite Oceanographic (AVISO) records. CI = 0.1 m

phase difference of the PDF became smaller (approaching to $\pi/5$) with decreasing periods of fluctuation. It would be expected that this phase difference shift could express the time-scale boundary between hypotheses of phase differences $\pi/2$ and $\pi/4$ discussed in Sect. 3.1.4. However, due to the 3-day running window in the AMSR-E SST data processing and the Reynolds weekly SST used in the MERRA reanalysis processing, it is not possible to discuss the phase difference shift precisely from $\pi/2$ to $\pi/5$ (less than about 5-day differences) in the shorter period band from these datasets.

In intra-annual (100- to 200-day period) band, a moderate fraction of the coherent variances between $Q_{\text{net}}^{\downarrow}$ and SST showed negative phase difference, which means that the upward NHF from the sea surface was large (small) when SST was high (low). This negative phase differences appeared in a specific season and location. In the Kuroshio, Kuroshio recirculation region, and Kuroshio/Oyashio Mixed Water Region (Fig. 4a–c), negative phase difference cores were found in the intra-annual band. On the other hand, cores of phase differences were located in the $[0, \pi/2]$ in the subtropical and subpolar oceans (Fig. 4e). Figure 6 shows the frequency distribution of the coherence variation in the phase-difference–season space, for a 157-day period. Ellipses with black lines are the result of EM+GMM clustering with cluster number $K = 5$, in which the BIC has a local minimum value. A remarkable cluster, hereafter called cluster A, was found from February to May, with a negative phase difference at $[-\pi, -\pi/3]$. The relative weight W_l of this cluster A to the total number was 16.6 %. Figure 7 shows the spatial distribution of the appearance probability of elements (ratio of the duration of this phenomenon and the total duration) belonging to this cluster A

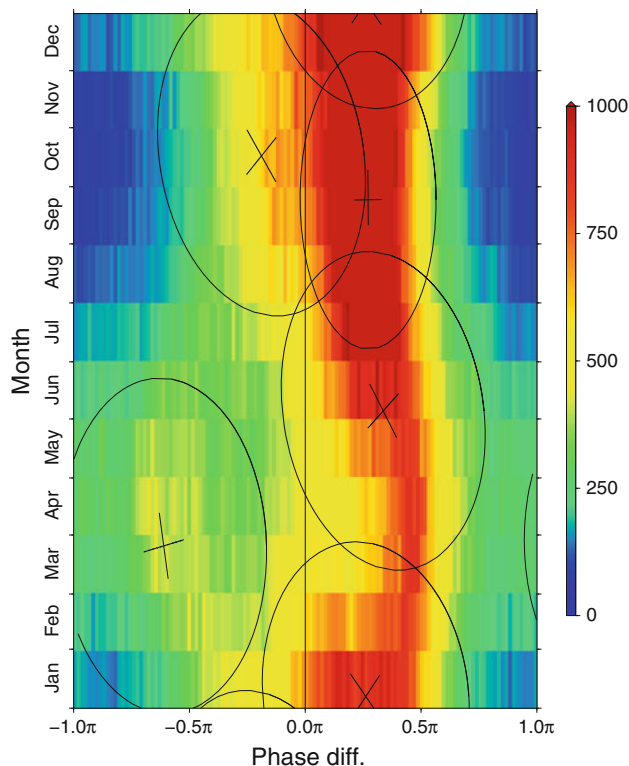


Fig. 6 Frequency diagram for 157-day period band on month and phase difference $\delta\theta$ space. The colors show the data in each $\pi/72$ -phase \times 1-month bin. The ellipses and their axis (indicated by black lines) indicate the centers and core areas of each cluster, derived from the EM + GMM method. The core area of the cluster is defined as $1/2(\mathbf{x} - \mu_l)^T \Sigma_l^{-1} (\mathbf{x} - \mu_l) \leq 1$ in Eq. (20)

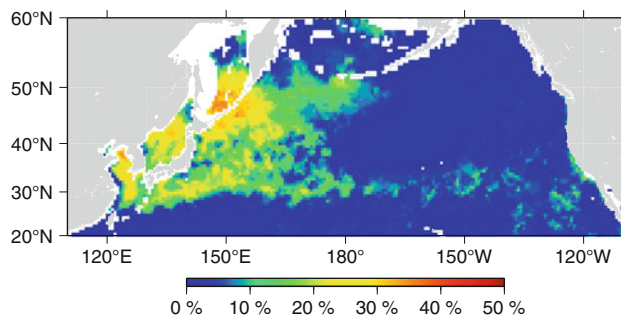


Fig. 7 Spatial incidence distribution of the negative phase-difference cluster on each grid in a 157-day period band

in each grid. These phenomena frequently occurred in the western North Pacific and its marginal seas (East China Sea, Japan Sea and Okhotsk Sea). The areas with especially high probability, up to 40 %, were these marginal seas, recirculation regions and the adjacent areas of the Kuroshio, the Kuroshio Extension, and the Oyashio. The small core was located at 30°N , 170°E . Another core with moderate probability was found at $25\text{--}30^{\circ}\text{N}$, $160\text{--}130^{\circ}\text{W}$ in the central North Pacific. Figure 8 shows the PDFs of the

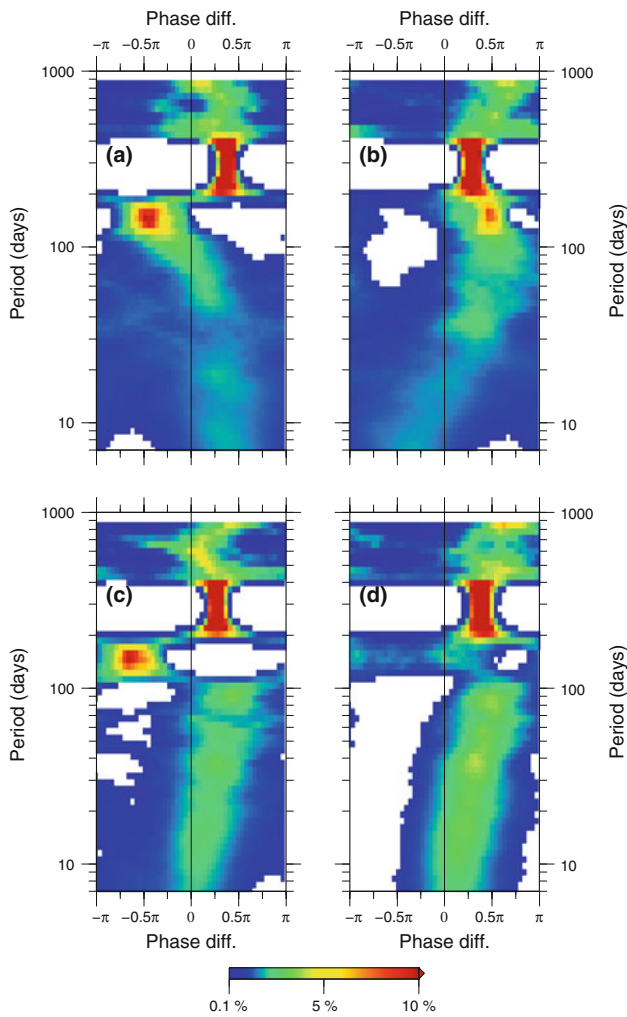


Fig. 8 Frequency diagram of the phase difference between the downward heat and radiation fluxes and SST for areas in which the incidence of cluster A (Fig. 7) is above 15%. **a** downward net shortwave radiation (Q_{SWn}^{\downarrow}), **b** downward net longwave radiation (Q_{LWn}^{\downarrow}), **c** downward sensible heat flux ($-Q_{SH}^{\downarrow}$), and **d** downward latent heat flux ($-Q_{LH}^{\downarrow}$)

phase relationship between the four components of the downward NHF (Q_{SWn}^{\downarrow} , Q_{LWn}^{\downarrow} , $-Q_{SH}^{\downarrow}$ and $-Q_{LH}^{\downarrow}$) and SST in the area where the appearance probability of the cluster A was above 15%. A high probability of negative phase differences between flux and SST, which means that the upward flux component was large (small) when SST was high (low), was found in the intra-annual band for shortwave radiation and sensible heat flux. A small probability of phase differences around $-\pi$ appeared in the intra-annual band for the latent heat flux. At the intra-annual band, the variance ratios of the four components compared to Q_{net}^{\downarrow} in the areas with especially high probability of Q_{net}^{\downarrow} -SST negative phase differences were $|Q_{SWn}^{\downarrow}|^2/|Q_{net}^{\downarrow}|^2 = 66.4\%$, $|Q_{LWn}^{\downarrow}|^2/|Q_{net}^{\downarrow}|^2 = 29.0\%$, $|Q_{SH}^{\downarrow}|^2/|Q_{net}^{\downarrow}|^2 = 23.5\%$, and $|Q_{LH}^{\downarrow}|^2/|Q_{net}^{\downarrow}|^2 = 45.4\%$, respectively. It suggests that the shortwave radiation might be associated with

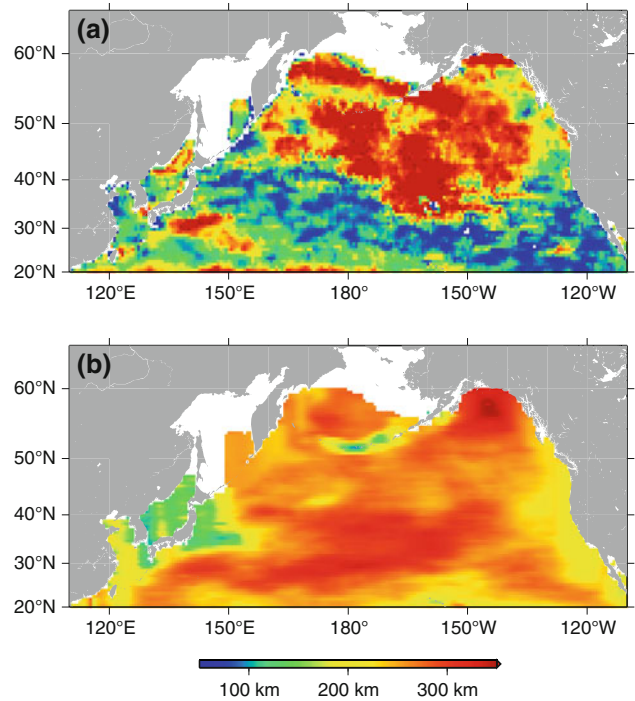


Fig. 9 Zonal decorrelation scales of SST variations: **a** intra-annual (100- to 200-day period bands) SST variation, **b** weekly to intra-seasonal (<100-day period bands) SST variation

the negative phase relationship between Q_{net}^{\downarrow} and SST at the intra-annual band in the area.

The zonal spatial scale of the SST in the intra-annual (100- to 200-day periods) band, which was extracted from the original SST time series using a wavelet filter at each grid, was distributed as shown in Fig. 9a. In the area where the negative phase differences were often found, the spatial scale was about 50–150 km. Therefore, it is reasonable to suppose that the SST disturbances in the intra-annual band generally had mesoscale oceanic features, where the SST and Q_{net}^{\downarrow} frequently had negative phase relationships. An exception is the Kuroshio recirculation region, in which the zonal scale was around 300 km. Then, it is suggested that the intra-annual variability of the SST in the recirculation region would fluctuate over the extensive spatial scale. In other areas, where the negative phase differences between Q_{net}^{\downarrow} and SST were not frequent in the intra-annual band, the zonal scales were over 200 km. Figure 4d, e show that the phase differences in these mid-oceans were around $[0, \pi/2]$, indicating the SST controlled by atmospheric forcing (NHF). The zonal spatial scales for shorter (less than 100-day period) band, shown in Fig. 9b, were from 200 to 350 km in most of the North Pacific.

It suggests that SST variability at the shorter band might be controlled by atmospheric disturbances, whose spatial scales would be significantly larger than those of oceanic

disturbances. This was also suggested by phase difference between $Q_{\text{net}}^{\downarrow}$ and SST (Figs. 3, 4).

The small zonal scales in the range of 100–200 km were distributed in the Japan Sea, the Yellow Sea, the Kuroshio/Oyashio Mixed Water Region, and the coastal oceans of the Aleutian Islands. In these areas, it is suggested that small-scale perturbations with short temporal periods would be active, as compared to other areas in the North Pacific. The relatively small-scale perturbations in atmosphere would be dominant in these coastal and marginal seas, due to land influence on the atmospheric disturbances.

5 Summary and discussion

The local phase relationship between the NHF and SST in the North Pacific was investigated. By employing the wavelet transform method, relationships at various temporal scales over weekly to annual cycle were simultaneously revealed. In this study, a positive phase difference was defined to indicate that the change of downward NHF leads that of SST; NHF would control the SST variations at the given time scale and duration.

In the annual cycle, it was suggested that the NHF would predominantly control SST change, which was indicated by the positive phase difference around $[\pi/5, \pi/2]$. The positive phase differences were also predominant in weekly to intra-seasonal (less than 100-day period) bands. On the other hand, in the intra-annual (100- to 200-day periods) bands, a part of the coherent variation between two parameters showed negative phase differences, which suggested that SST changes would affect the air–sea interaction, in the western North Pacific and winter-to-spring seasons. The spatial scales in these intra-seasonal and intra-annual bands were found to be contrasting; the former was over 200 km except for the Japan Sea and Kuroshio/Oyashio Mixed Water Region, while the latter, where the negative phase differences were frequently found, ranged from 50 to 150 km. The results shown here would be associated with the seasonal dependencies found in the decorrelation scale of the SST anomaly by Hosoda and Kawamura (2004, 2005). Vallis (2006) noted that, with a typical deformation radius in the atmosphere of 1,000 km, non-dimensional frequency of unity for Rossby wave in the atmosphere corresponds to a period of about 7 days. In the mid-latitude ocean with a deformation radius of 50 km, a non-dimensional frequency of unity for Rossby wave in the oceans corresponds to a dimensional period of about 100 days. Non-dimensional velocities of unity correspond to respective dimensional velocities of about 0.25 ms^{-1} (ocean) and 10 ms^{-1} (atmosphere). Since SST fields are affected by both atmospheric and oceanic disturbances in parallel, it would be reasonable that the

discrepancy of spatial scales in SST variations were found between the intra-seasonal and intra-annual bands mentioned above. It can be concluded that the clear disparity between the intra-seasonal and intra-annual variations would be helpful for determining at least one of the appropriate cut-off frequencies for the scale-dividing method in the OI procedure for SST.

The phenomena of SST variability in time and fluctuation periods are highly dependent on the analyzed areas. Therefore, the results shown in this study for the North Pacific would not be applicable for other oceans. For example, the eastern tropical Pacific, in which it is well known that the SST changes air–sea interactions, would have different temporal characteristics for SST and heat flux changes. The appropriate cut frequency for the scale-dividing method should be obtained by individual analysis for each ocean, based on the method used in this study.

The spatial scales of SST temporal changes in the intra-annual bands suggests their association with the mesoscale variability in the oceans, including mesoscale eddies, meanders or path variations of currents, and vertical mixing. From altimetric observations of sea surface height (SSH) in the North Pacific, it has been reported in recent decades that mesoscale variability is active in the intra-seasonal to longer time scales. Adamec (1998) found modulation of the Kuroshio Extension with a time scale of 90–110 days. Ebuchi and Hanawa (2000) pointed out that the altimeter-derived SSH anomaly has a broad band of energy with several peaks at periods between 45 and 180 days. Kashima et al. (2009) showed that the Kuroshio path had quasi-periodic modulation by mesoscale eddies with 100- to 150-day time scales. Kobashi and Kawamura (2001) showed that the dominant temporal scale of the SSH in the subtropical gyre is 65–220 days, and that energetic area with this time scale is distributed in the western and central (elongated to 160°W in the south of 30°N) North Pacific. From SSH in the Kuroshio region, Schmeits and Dijkstra (2002) discussed the statistically significant propagating mode of variability with a time scale of 7 months. The SST disturbances with intra-annual periods and spatial scales of O (100 km) derived in this study would be associated with the SSH variability revealed by previous studies.

Negative phase differences (around $-\pi$ to $-\pi/3$) between the downward NHF and the SST in the intra-annual bands, found in the wintertime western North Pacific, mean that the upward NHF reached a positive (negative) peak when the SST achieved a positive (negative) peak. This relationship suggests that the SST would affect NHF changes, since the SST should decrease when upward NHF was positive, under the condition of NHF dominance of the air–sea interaction. While in most of the mid-latitude oceans NHF variability is controlled by the

atmosphere (Cayan 1992; Frankignoul and Kestenare 2002), it has been pointed out that the ocean heat content and SST become more important in determining anomalies of heat fluxes in the western boundary current regions (Frankignoul and Kestenare 2002; Tanimoto et al. 2003). Tokinaga et al. (2009) reported from in situ and satellite observations that the heat release from winter sea surface caused strong vertical development of clouds in the southern flank of the Kuroshio Extension. Sugimoto and Hanawa (2011) reported that high SST anomalies with mesoscale structure detached from the Kuroshio Extension affect the NHF in the Kuroshio/Oyashio Mixed Water Region in wintertime. The negative phase difference cluster in this study would be consistent with these previous research. Especially, it seems reasonable that Tokinaga et al. (2009)'s results might be associated with one of the possible mechanisms for the negative phase differences between net shortwave radiation and SST found in this study.

In the EM + GMM clustering (Fig. 6), three consecutive clusters were estimated in the phase difference of $[0, \pi/2]$. Fundamentally, a more plausible clustering result would be to unify these three clusters into one cluster with large σ_{DY} , which would be comparable to the whole temporal length for DY (1 year). This hypothetical "appropriate" cluster combined from the analyzed three clusters would not have a structured outer side of a Gaussian equation in the season dimension (DY) because of the cyclic condition for DY. Since the EM + GMM clustering could not express the characteristics for such a long σ_{DY} cluster by one Gaussian function, the hypothetical "appropriate" cluster would be described by linear superposition of a few clusters, in which cluster number $K = 5$ including other clusters was optimum. The clustering method for cyclic dimensional data is required to be developed for this research.

This study investigated phase differences between NHF and SST under an assumption of their simple linear relationship using the wavelet transform method. Nonlinear processes, including temporal change of the depth scale $D(t)$ of Eq. (4) for Cayan's (1992) model, were not discussed. Since the depth scale $D(t)$ would depend on SST, the relationship between NHF and SST should be more complicated even in the cooling phase than Cayan's (1992) model. From the results revealed here, the future direction of this study will be one that encompasses both linear and nonlinear processes for describing heat content change in upper ocean.

Because of the data processing (3-day running mean) in the AMSR-E SST and weekly OISST data used in the MERRA reanalysis, phenomena with time scales of less than a weekly period were not discussed in this study. In addition, smaller spatial scales of less than 50 km were not

available from these two datasets. Especially, atmospheric reanalysis data using at least moderate resolution O (50 km) of SST for boundary condition are required for permitting or resolving oceanic eddy fields to discuss the coherent and incoherent variation of heat fluxes and SST even in the intra-annual to shorter period bands. The latest Reynolds OISST (Reynolds et al. 2007) dataset, based on AMSR-E and AVHRR blended data, is one of the candidates for the more appropriate boundary conditions (Appendix). For similar reasons, a detailed discussion of weekly to monthly time scales, in which the phase differences shifted to smaller phase difference in shorter time scales, could not be undertaken in this study. Advection heat transport by geostrophic and non-geostrophic (e.g., Ekman) currents and vertical effects with dissipation were also not fully considered to simplify the analysis. To discuss these remaining problems, including the heat transport effect by poleward currents, suggested by phase difference map of annual cycle, and the driving mechanism in the SST-leading changes in the wintertime on the intra-annual time scale, three-dimensional data with higher spatial and temporal resolution for both oceanic and atmospheric fields are required.

Acknowledgements The author would like to express gratitude to members of physical oceanographic and satellite oceanographic groups in Tohoku University for their helpful comments and advices. Two anonymous reviewers gave valuable comments and suggestions to significantly improve this manuscript. The Japan Aerospace Exploration Agency (JAXA) Earth Observation Research Center (EORC) is thanked for providing AMSR-E SST data. The Global Modeling and Assimilation Office (GMAO) and the GES DISC are thanked for for the dissemination of MERRA heat flux data.

Appendix: Difference between Reynolds OISST and AMSR-E un-filtered SST

The MERRA used weekly- and 1° -resolution OISST product of Reynolds et al. (2002) for boundary condition of the ocean surface. It is suggested that the low resolution with optimal interpolation using large de-correlation scales would blur mesoscale structures of ocean surface. Figure 10 shows the spatial distributions of root-mean-square difference (RMSD) between Reynolds OISST and AMSR-E SST. The SST differences were calculated using data from January 1, 2003 to December 31, 2010. The 3-day running mean were adopted for AMSR-E SST to fulfill the gaps in the dataset. Two Reynolds OISST datasets were compared with the AMSR-E SST: (1) the previous version Reynolds OISST (RSST02; Reynolds et al. 2002, weekly, 1° resolution), which was used for boundary condition in MERRA, and (2) the latest version Reynolds OISST based on blended AVHRR and AMSR-E (RSST07;

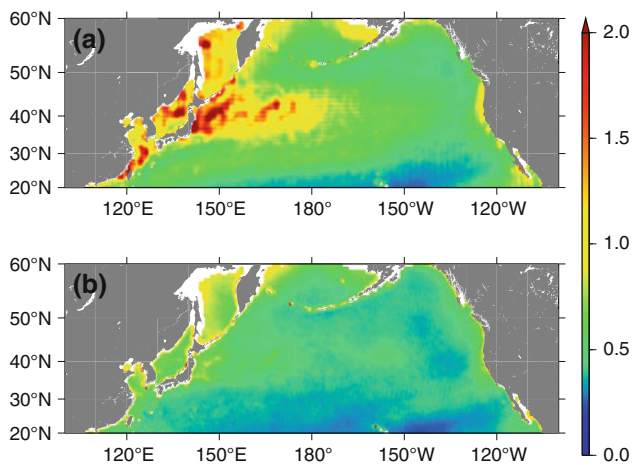


Fig. 10 Root-Mean-Square Difference (RMSD: Unit °C) between Reynolds OISST data and AMSR-E 3-day mean SST. **a** Reynolds weekly AVHRR-only OISST (Reynolds et al. 2002), **b** Reynolds daily AVHRR+AMSR-E blended OISST (Reynolds et al. 2007)

Reynolds et al. 2007, daily, 0.25° resolution). For RSST02, nearest-neighbor method was adopted for interpolating low-resolution SST data into AMSR-E grid (daily, 0.25°) before comparison. Large differences between RSST02 and AMSR-E SST, which were up to 2.0°C , were found in the western North Pacific, especially at the northern side of the SST fronts (the Kuroshio in the eastern China Sea, subarctic front in the Japan Sea, and Kuroshio/Oyashio Mixed Water Region). Even if the monthly averaging without spatial smoothing was adopted for both RSST02 and AMSR-E SST datasets, these SST differences in the western North Pacific were reduced by only $0.2\text{--}0.4^\circ\text{C}$ (figure not shown). Therefore, it is suggested that the difference would be due to low spatial resolution in RSST02, which might affect the estimation of flux variability even in low-frequency bands.

In the comparison between RSST07 and AMSR-E SST, these differences were reduced to 1.0°C or less. It could be expected that the atmospheric reanalysis products using the AMSR-E and AVHRR blended RSST07 would improve their estimation of ocean surface fluxes in the near future.

References

- Adamec D (1998) Modulation of the seasonal signal of the Kuroshio Extension during 1994 from satellite data. *J Geophys Res* 103:10209–10222
- Bilmes J (1998) A gentle tutorial on the EM algorithm and its application to parameter estimation for Gaussian mixture and hidden Markov models. Technical report, Technical Report ICSI-TR-97-02. University of Berkeley
- Brunke MA, Wang Z, Zeng X, Bosilovich M, Shie C-L (2011) An assessment of the uncertainties in ocean surface turbulent fluxes

- in 11 reanalysis, satellite-derived, and combined global datasets. *J Clim* 24:5469–5493
- Cayan DR (1992) Latent and sensible heat flux anomalies over the Northern Oceans: driving the sea surface temperature. *J Phys Oceanogr* 22:859–881
- Chou C, Hsueh Y-C (2010) Mechanisms of northward-propagating intraseasonal oscillation—a comparison between the Indian Ocean and the western North Pacific. *J Clim* 23:6624–6640
- Deser C, Timlin MS (1997) Atmosphere–ocean interaction on weekly timescales in the North Atlantic and Pacific. *J Clim* 10:393–408
- Ebuchi N, Hanawa K (2000) Mesoscale eddies observed by TOLEX/ADCP and TOPEX/POSEIDON altimeter in the Kuroshio recirculation regions south of Japan. *J Oceanogr East Pac* 56:43–57
- Emery WJ, Thomson RE (2001) Data analysis methods in physical oceanography, 2nd and revised edn. Elsevier, Amsterdam
- Eyre J, Andersson E, Charpentier E, Ferranti L, Lageuille J, Ondras M, Paillex J, Rabier F, Riishojgaard LP (2009) Requirements of numerical weather prediction for observations of the oceans. In: Hall J, Harrison D, Stammer D (eds) Proceedings of OceanObs'09: Sustained Ocean Observations and Information for Society, vol 2. ESA Publication WPP-306. Venice, Italy. doi:10.5270/OceanObs09.cwp.26
- Frankignoul C, Kestenare E (2002) The surface flux feedback. Part I: estimate from observations in the Atlantic and the North Pacific. *Clim Dyn* 19:633–647
- Fu R, Liu WT, Dickinson RE (1996) Response of tropical clouds to the interannual variation of sea surface temperature. *J Clim* 9:616–634
- Gill AE, Turner JS (1976) A comparison of seasonal thermocline modes with observation. *Deep Sea Res* 23:391–401
- Grinsted A, Moore JC, Jevrejeva S (2004) Application of the cross wavelet transform and wavelet coherence to geophysical time series. *Nonlinear Proc Geophys* 11:561–566
- Guan L, Kawamura H (2004) Merging satellite infrared and microwave SSTs: methodology and evaluation of the new SST. *J Oceanogr* 60:905–912
- He R, Weisberg RH, Zhang H, Muller-Karger FE, Helber RW (2003) A cloud-free, satellite-derived, sea surface temperature analysis for the West Florida Shelf. *Geophys Res Lett* 30. doi:10.1029/2003GL017673
- Hickey BM (1989) Patterns and processes of circulation over the Washington continental shelf and slope. In: Landry M, Hickey B (eds) Oceanography of the Washington–Oregon coastal zone. Elsevier, Amsterdam, pp 41–109
- Hosoda K (2010) A review of satellite-based microwave observations of sea surface temperatures. *J Oceanogr* 66:439–473
- Hosoda K, Kawamura H (2004) Global space-time statistics of sea surface temperature estimated from AMSR-E data. *Geophys Res Lett* 31. doi:10.1029/2004GL020317
- Hosoda K, Kawamura H (2005) Seasonal variation of space/time statistics of short-term sea surface temperature variability in the Kuroshio region. *J Oceanogr* 61:709–720
- Iwasaki S, Kubota M, Tomita H (2008) Inter-comparison and evaluation of global sea surface temperature products. *Int J Remote Sens* 29:6263–6280
- Kashima M, Ito S-I, Ichikawa K, Imawaki S, Umatani S-I, Uchida H, Setou T (2009) Quasiperiodic small meanders of the Kuroshio off Cape Ashizuri and their inter-annual modulation caused by quasiperiodic arrivals of mesoscale eddies. *J Oceanogr* 65:73–80
- Kawai Y, Kawamura H, Takahashi S, Hosoda K, Murakami H, Kachi M, Guan L (2006) Satellite-based high-resolution global optimum interpolation sea surface temperature data. *J Geophys Res* 111. doi:10.1029/2005J003313
- Kobashi F, Kawamura H (2001) Variation of sea surface height at periods of 65–220 days in the subtropical gyre of the North Pacific. *J Geophys Res* 106:26817–26831

- Konda M, Imasato N, Shibata A (1996) Analysis of the global relationship of biennial variation of sea surface temperature and air–sea heat flux using satellite data. *J Oceanogr* 52:717–746
- Liu WT, Zhang A, Bishop JKB (1994) Evaporation and solar irradiance as regulators of sea surface temperature in annual and interannual changes. *J Geophys Res* 99:12623–12637
- McClain EP, Pichel WG, Walton CC (1985) Comparative performance of AVHRR-based multichannel sea surface temperatures. *J Geophys Res* 90:11,587–11,601
- Murakami H, Kawamura H (2001) Relations between sea surface temperature and air–sea heat flux at periods from 1 day to 1 year observed at ocean buoy stations around Japan. *J Oceanogr* 57:565–580
- Pelleg D, Moore A (2000) X-means: extending K-means with efficient estimation of the number of clusters. In: *Proc. 17th International Conference on machine learning (ICML'00)*. pp 727–734
- Reynolds RW, Smith TM (1994) Improved global sea surface temperature analyses using optimum interpolation. *J Clim* 7:929–949
- Reynolds R, Rayner NA, Smith TM, Stokes DC, Wang W (2002) An improved in situ and satellite SST analysis for climate. *J Clim* 15:1609–1625
- Reynolds RW, Smith TM, Liu C, Casey DBCKS, Schlax MG (2007) Daily high-resolution-blended analyses for sea surface temperature. *J Clim* 20:5473–5496
- Rienecker MM, Suarez MJ, Gelaro R, Todling R, Bacmeister J, Liu E, Bosilovich MG, Schubert SD, Takacs L, Kim G-K, Bloom S, Chen J, Collins D, Conaty A, da Silva A, Gu W, Joiner J, Koster RD, Lucchesi R, Molod A, Owens T, Pawson S, Redder PPCR, Reichle R, Robertson FR, Ruddick AG, Sienkeiwicz M, Woollen J (2011) MERRA: NASA's modern-era retrospective analysis for research and applications. *J Clim* 24:3624–2648
- Sakaida F, Kawamura H, Takahashi S, Shimada T, Kawai Y, Hosoda K, Guan L (2009) Research, development, and demonstration operation of the new generation sea surface temperature for open ocean (NGSST-O) product. *J Oceanogr* 65:859–870
- Sakurai T, Kurihara Y, Kuragano T (2005) Merged satellite and in-situ data global daily SST. In: *Proceedings of 2005 IEEE International geoscience and remote sensing symposium, IGARSS '05*, vol 4. pp 2606–2608
- Schmeits MJ, Dijkstra HA (2002) Subannual variability of the ocean circulation in the Kuroshio region. *J Geophys Res* 107. doi: [10.1029/2001JC0011073](https://doi.org/10.1029/2001JC0011073)
- Schwarz GE (1978) Estimating the dimension of a model. *Ann Stat* 6:461–464
- Shibata A (2004) AMSR/AMSR-E SST algorithm developments—removal of ocean wind effect. *Italian J Remote Sens* 30/31: 131–142
- Shibata A (2006) Features of ocean microwave emission changed by wind at 6 GHz. *J Oceanogr* 62:321–330
- Shibata A (2007) Effect of air–sea temperature difference on ocean microwave brightness temperature estimated from AMSR, SeaWinds, and buoys. *J Oceanogr* 63:863–872
- Shinoda T, Hendon HH, Glick J (1998) Intraseasonal variability of surface fluxes and sea surface temperature in the tropical western Pacific and Indian Oceans. *J Clim* 11:1685–1702
- Sugimoto S, Hanawa K (2011) Roles of SST anomalies on the wintertime turbulent heat fluxes in the Kuroshio–Oyashio confluence region: influences of warm eddies detached from the Kuroshio Extension. *J. Clim* 15:6551–6561
- Tanimoto Y, Nakamura H, Kagimoto T, Yamane S (2003) An active role of extratropical sea surface temperature anomalies in determining anomalous turbulent heat flux. *J Geophys Res* 108. doi:[10.1029/2002JC001750](https://doi.org/10.1029/2002JC001750)
- Thorpe SA (2007) *An Introduction to ocean turbulence*. Cambridge University Press, Cambridge
- Tokenaga H, Tanimoto Y, Xie S-P, Tomita H, Ichikawa H (2009) Ocean frontal effects on the vertical development of clouds over the western North Pacific: in situ and satellite observations. *J Clim* 22:4241–4260
- Torrence C, Compo G (1998) A practical guide to wavelet analysis. *Bull Am Meteorol Soc* 79:61–78
- Torrence C, Webster PJ (1999) Interdecadal changes in the ENSO-monsoon system. *J Clim* 12:2679–2690
- Vallis GK (2006) *Atmospheric and oceanic fluid dynamics: fundamentals and large-scale circulation*. Cambridge University Press, Cambridge
- Wallace JM, Smith C, Jiang Q (1990) Spatial patterns of atmosphere–ocean interaction in the northern winter. *J. Clim* 3:990–998
- Wang C, Enfield DB (2001) The tropical western hemisphere warm pool. *Geophys Res Lett* 28:1635–1638
- Wang L, Li T, Zhou T (2012) Intraseasonal SST variability and air–sea interaction over the Kuroshio Extension region during boreal summer. *J Clim* 25:1619–1634
- Warren BA (1976) Insensitivity of subtropical mode water characteristics to meteorological fluctuations. *Deep Sea Res* 19:1–19
- Wu R, Kinter JL III (2010) Atmosphere–ocean relationship in the midlatitude North Pacific: seasonal dependence and east–west contrast. *J Geophys Res* 115. doi:[10.1029/2009JD012579](https://doi.org/10.1029/2009JD012579)